

Energy/Delay Tradeoffs in All-Spin Logic Circuits

Zhaoxin Liang and Sachin S. Sapatnekar, *Fellow, IEEE*

Abstract—All-spin logic (ASL) is a spin-based candidate for implementing logic in next generation designs. The energy and delay of ASL circuits are both inherently related to the geometric parameters of ASL gates, and careful selection of the dimensions for ASL gates is required to achieve optimal performance. In this work, a trade-off relation between energy and delay is explored to optimally size the magnets and channels in an ASL gate to provide an optimal balance under various delay and energy demands. Results on optimizing interconnects and benchmark circuits are presented.

Index Terms—All-spin logic, spintronics, sizing, optimization.

I. INTRODUCTION

Spin-based computing is a post-CMOS technology candidate that has recently seen an increased research focus. For spin-based logic, nonlocal spin transfer devices are very promising, particularly All-Spin Logic (ASL) [1]–[7].

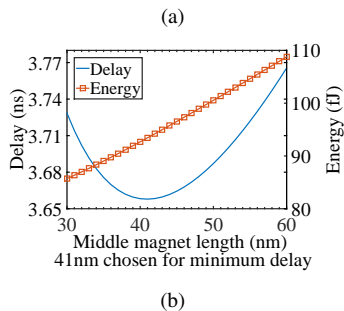
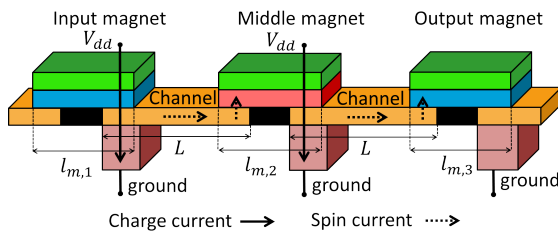


Fig. 1. (a) A three-magnet/two-channel ASL circuit. (b) Its energy and delay.

In this paper, we study methods for improving the performance of ASL circuits through careful selection of the dimensions of circuit elements, resulting in energy-delay tradeoffs. To motivate the problem, consider an ASL structure with three magnets connected by two separated channels in Fig. 1(a). We fix the dimensions of the input/output magnets and examine the energy and delay impact of changing the length, $l_{m,2}$, of the middle magnet, temporarily assuming that this value can be varied continuously. Increasing $l_{m,2}$ increases energy at both the input and output sides. However,

the delay impact is nonmonotonic: the time required to switch the middle magnet increases because a larger magnet requires more spin torque, but the switching time of the output magnet reduces since a larger middle magnet can deliver more spin torque. Thus, there is an overall energy/delay trade-off relation, as shown in Fig 1(b). Further, the choice of channel length also affects switching speed in such nonlocal spin valve structures [8]–[10], implying that buffer insertion in a long interconnect can help in reducing wire delays.

The major contribution of our work is in developing and assembling a modeling and optimization framework for performance optimization of general ASL circuits through magnet sizing and buffer insertion, and the demonstration of the energy/delay trade-off relation during the optimization. We introduce energy and delay models for ASL circuits (Section II) and show the impact of geometric parameters on performance (Section III). An optimization problem formulation is proposed (Section IV) to obtain energy-delay tradeoffs. We show results on a long interconnect line and large benchmarks under multiple technologies (Section V) and conclude in Section VI.

II. ASL PERFORMANCE MODELING

A. Structure of a basic ASL gate

A basic ASL gate [1] consists of three major components as shown in Fig. 2: an input magnet at left that polarizes the charge current and injects spin current into the channel, a channel that transfers the spin current from input magnet to output magnet, and an output magnet that sets its state based on the incoming spin torque. A metal contact, connected to the supply voltage, lies above each magnet, and a ground connection is placed beneath the input end of the channel. To allow a magnet to serve both as output to its previous magnet and input to its following magnet, an isolation feature is placed under it, separating the part of the channel beneath the magnet into two segments – an input and an output side – thus ensuring that the input and output spin currents interact minimally. Since this is a drawn feature, its size is constrained by lithography and corresponds to the minimum feature size.

For the ASL inverter in Fig. 2, at the input side, a charge current (solid arrow) flows from V_{dd} to ground. The polarizing action of the input magnet results in a spin accumulation, opposite to the magnet spin, at the input end and this diffuses towards the output (dotted arrow), creating a spin torque at the output end that sets the output magnet state. A buffer is similar in structure, except that the role of V_{dd} and ground are interchanged: this ensures that the input magnet introduces a spin current of the same polarity into the channel.

B. An analytical model for switching delay in ASL circuits

For the gate in Fig. 2, annotated with its geometrical parameters, we consider each contributor to switching: spin current

generation at the input, non-local spin transport through the channel, and spin-torque-based switching at the output.

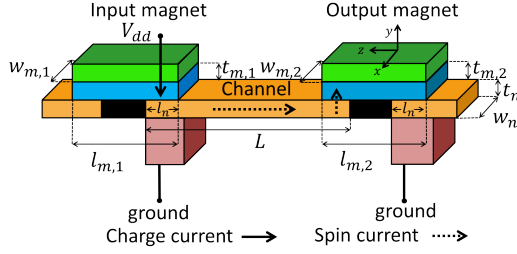


Fig. 2. Structure of a basic ASL gate.

1) *Charge current at the input magnet:* The injected charge current is converted to spin current at the input end of the channel. For the structure in Fig. 2, the positioning of the ground terminal on the input side, along with the presence of the isolation feature, introduces an asymmetry that causes charge current, I_c , to be injected to the input side, given by:

$$I_c = \frac{V_{dd}}{R_s + R_m + R_n + R_g} \quad (1)$$

where R_s , R_m , R_n , and R_g indicate the resistance of the contact to supply voltage, magnet, channel, and ground connection, respectively, on the input side. The parasitics of both the supply and ground connections are included in the R_s and R_g , ensuring that the ohmic loss associated with power and ground distribution are incorporated in our models. The other two quantities, R_m and R_n , can be calculated as:

$$R_m = \frac{\rho_F t_m}{A_{F,1}/2}, \quad R_n = \frac{\rho_N t_n}{w_n \cdot l_n} \quad (2)$$

where $A_{F,1} = w_{m,1} l_{m,1}$ is the interface area between the magnet and contact, with width $w_{m,1}$ and length $l_{m,1}$. The factor of 2 indicates that only half of the magnet is effectively available for injecting charge/spin current; the other half receives spin current from the gate that drives this magnet. The area $A_N = w_n \cdot l_n$ between the magnet and channel is used for calculating the channel resistance. The parameters ρ_F and ρ_N are the resistivity of magnet and channel, and t_m and t_n are the thickness of magnet and channel, respectively.

2) *Spin transfer through the channel:* The charge current at the input magnet is transformed into a spin current at the source end, which drifts down towards an output magnet through a lossy interconnect medium. We capture these factors and arrive at an expression for the input–output delay of an ASL gate. For a single fanout structure, i.e., a channel without branches, such as an ASL inverter or buffer, the spin current can be calculated by an analytical expression for the spin injection efficiency, while in more complicated structures with multiple fanouts, the spin current at each output can be evaluated using numerical computations [6].

The spin injection efficiency, η , is the ratio of the spin current, I_s , at the end of the channel to the injected charge current, I_c . In a single-fanout structure, η is given by [2], [11]:

$$\eta = \frac{I_s}{I_c} = \frac{e^{-L/\lambda_N} x_1 P_1}{(1 + x_1)(1 + x_2) - e^{-2L/\lambda_N}}, \quad (3)$$

where L is the length along the channel from the point of injection of spin current at the input magnet to the channel region below the output magnet, and λ_N is the spin diffusion length of the channel. The terms x_1 and x_2 are defined as:

$$x_1 = \frac{2R_1}{R_N(1 - P_1^2)}, \quad x_2 = \frac{2R_2}{R_N(1 - P_2^2)}, \quad (4)$$

where P_1 and P_2 are the polarization factors for the input and output magnets, respectively, R_1 and R_2 are the spin accumulation resistances for the input and output magnet, respectively, and R_N is the spin accumulation resistance of the channel. These terms are given by:

$$R_{\{1,2\}} = \frac{\rho_F \lambda_F}{A_{F\{1,2\}}/2} = \frac{2\rho_F \lambda_F}{w_{m\{1,2\}} \cdot l_{m\{1,2\}}}, \quad (5)$$

$$R_N = \frac{\rho_N \lambda_N}{A_N} = \frac{\rho_N \lambda_N}{w_n \cdot t_n} \quad (6)$$

with λ_F and λ_N standing for the spin diffusion lengths and ρ_F and ρ_N being the resistivities, with subscripts F and N for the ferromagnet and channel, respectively.

C. Switching the output magnet

The Landau-Lifschitz-Gilbert (LLG) [12] equation describes the magnet switching dynamics due to a spin current:

$$\frac{d\vec{m}}{dt} = -[\gamma|\vec{m} \times \vec{H}_{eff} + \alpha\vec{m} \times \frac{d\vec{m}}{dt} - \frac{1}{qN_s}\vec{m} \times (\vec{m} \times \vec{I}_s)] \quad (7)$$

Vector \vec{m} indicates the normalized magnetization and changes from 1 to -1 or the opposite during switching over a time variable t , γ is the gyromagnetic ratio, α is the Gilbert damping coefficient, q is the electron charge, and N_s is the net number of Bohr magnetons of the magnet to be switched. The effective magnetization field, \vec{H}_{eff} , consists of the uniaxial anisotropy field \vec{H}_k and demagnetizing field \vec{H}_d . For in-plane magnet structures, \vec{H}_k is dominated by \vec{H}_d .

A complete analysis of the LLG equation is computationally intensive, especially within the inner loop of an optimizer. However, the equation can be used to infer information about the switching time t_{sw} under a spin torque switching current in a computationally inexpensive way. From Equation (3), writing the spin current at the end of the channel as $I_s = \eta I_c$, the switching time of the gate is given by [2].

$$t_{sw} = 2f_{sw}qN_s/(\eta I_c) \quad (8)$$

where I_c is given by Equation (1). The factor f_{sw} captures the fact that the spin current is partly responsible for switching, and the switching event also includes contributions from other related fields. In [2], f_{sw} was considered over a single magnet size, but our optimizer requires f_{sw} over a range of magnet sizes. In Section III-C, we will show that f_{sw} is well approximated as a constant over a wide range of magnet sizes.

1) *Delay in multifanin/multifanout structures:* General ASL gates are based on majority logic and involve more complex structures than that in Fig. 2. For example, Fig. 3(a) represents an ASL NAND gate with two fanouts, and the channel has multifanin and multifanout substructures. For such structures, there is no known simple analytical form for the spin current, analogous to Equation (3), at the output magnet(s). However,

the spin current at each output magnet can be calculated numerically by dividing the channel into wire segments [6].

Specifically, each component in the circuit – the input and output magnets as well as channel segments – can be described as a π -network of conductance matrices. By considering each logic stage separately, we divide this into two substructures and based on the π structures for each stage, illustrated in Fig. 3(b), we form a modified nodal analysis (MNA) matrix for the system and solve the resulting set of equations to obtain the charge and spin currents at any nodes. The currents injected into output magnets are then used to compute the spin injection efficiency, replacing the closed form in Equation (3), and the remainder of the process of computing t_{sw} is identical to the single-fanout case. A complete description of this interconnect model, along with a comparative evaluation against the analytical model, is provided in the Supplementary Material.

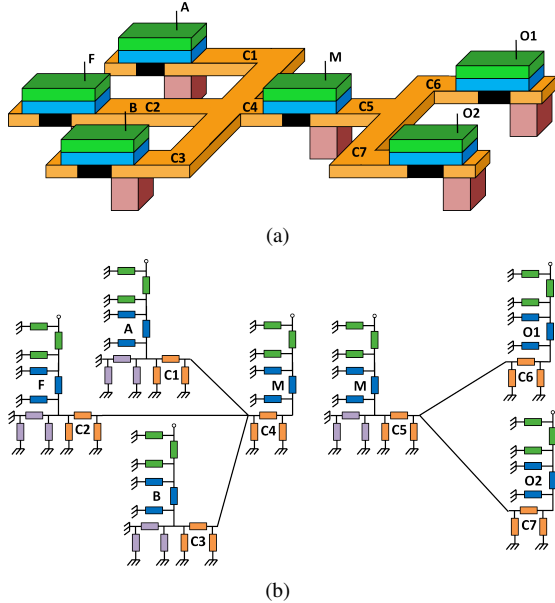


Fig. 3. (a) A two-input ASL NAND gate with two fanouts [6] and (b) its lumped circuit model.

2) *From gate delays to circuit delays*: Computing circuit delays from gate delays is a relatively straightforward process. As in static timing analysis for CMOS circuits, once the delays of each logic stage (i.e., a gate and its fanout interconnect) are computed using techniques described earlier in this section, a topological traversal from the primary inputs to the primary outputs can be used to find the delay of the circuit.

D. Modeling ASL switching energy

For any single-fanout or multifanout structure, the energy that is supplied comes from the V_{dd} source. Over a switching period, T , the total energy E for the gate is given by [2] as $E = V_{dd}I_cT$. Note that the energy dissipation can be attributed to the charge current, and the spin diffusion current and spin torque at the output are a consequence of the charge current. Therefore, for a logic circuit consisting of an interconnection of gates, the energy can be computed as:

$$E = \sum_{\text{all magnets } i} V_{dd}I_{c,i}T \quad (9)$$

where $I_{c,i}$ is the charge current injected into the magnet i .

III. IMPACT OF ASL GEOMETRIES

From the analysis of the energy and delay models in Section II, it can be seen that the dimensions of the magnets enter into several expressions. We now analyze the impact of geometry choices on circuit performance, specifically focusing on *optimizable layout parameters*: the magnet length and the channel length. We assume that technology-specific parameters such as the magnet thickness or channel thickness are fixed. We consider each component of switching one by one. For illustration, we will primarily consider the ASL inverter in Fig. 2: the quantities associated with the input and output magnet are represented with the subscript 1 and 2, respectively.

A. Influence on charge current injection

The dependence of the injected charge current, $I_{c,1}$, and the geometry can be shown by combining Equations (1) and (2):

$$I_{c,1} = \frac{V_{dd}}{R_{s,1} + R_{n,1} + R_{m,1} + R_g} = \frac{V_{dd}}{r_1/l_{m,1} + r_2} \quad (10)$$

where r_1 and r_2 are constants that absorb terms other than the optimizable layout parameters listed above. The value of $I_{c,1}$ is directly related to the system energy, as indicated by Equation (9), and as we will see soon, also the delay.

B. Influence on non-local spin transfer

The charge current creates spin current that is transported across the channel to the output magnet. For the single-fanout ASL inverter, an analytical expression for the spin current at the output magnet can be derived based on spin injection efficiency η and charge current at the input magnet I_c as $I_s = \eta I_c$. From Equations (3), (4), and (10), the dependence of I_s on the magnet lengths and channel lengths is given by:

$$I_s = \frac{k_1 V_{dd} e^{-L/\lambda_N}}{\left[\left(1 + \frac{k_2}{l_{m,1}}\right) \left(1 + \frac{k'_2}{l_{m,2}}\right) - e^{-2L/\lambda_N} \right] (r_1 + r_2 l_{m,1})} \quad (11)$$

where k_1 , k_2 , and k'_2 are constants that absorb all fixed geometry parameters, which depend on technology-specific parameters, as well as material and physical constants.

This expression can be analyzed to understand how the spin current changes with the magnet and channel geometries in the ASL inverter. We focus on the optimizable layout parameters: the lengths of the input and output magnets, $l_{m,1}$ and $l_{m,2}$, and the length of the channel, L . It can be seen that

- Increases in $l_{m,1}$ and $l_{m,2}$ will result in a larger spin current at the output magnets. The increase with $l_{m,1}$ occurs because a larger input magnet has a smaller resistance and injects more charge current, resulting in larger spin current at the output magnet. A larger output magnet as the result of longer $l_{m,2}$ absorbs more spin current from the channel, improving η .
- A longer channel length, L , results in weakened spin current at the output magnet, i.e., spin diffusion becomes more inefficient with increasing channel length.

For the multifanin/multifanout case, these closed-form expressions cannot be used, but the impact of changing these parameters broadly follows the same trend as described above.

C. Influence on the switching of the output magnet

The spin current at the end of the channel switches the output magnet, as governed by the LLG equation, with an input-to-output switching delay as expressed in Equation (8), based on an integration of the LLG equation over time. We assume the magnet to be a single domain since macrospin simulation is a good approximation to reflect the switching time trends, as influenced by various factors [13].

This integration involves two geometry-dependent terms. The first is the net number of Bohr magnetons, N_s , of the output magnet is proportional to its volume through $N_s = M_s V / \mu_B$, with μ_B as the unit Bohr magneton. This factor appears and affects t_{sw} through Equation (8). The second is the demagnetizing field \vec{H}_d , an internal field related to the saturated magnetization, M_s , and demagnetizing factor, N_d , through the relation $\vec{H}_d = N_d M_s \vec{m}$. The demagnetizing factor N_d of a magnet is a function of its dimensions and shape. We follow the equation in [14] to calculate the demagnetizing field along all three axes for a rectangular prism in our LLG simulation. The effective anisotropy constant is calculated as $K = (N_{xx} - N_{yy})M_s^2/2$, with N_{xx} and N_{yy} being the demagnetizing factor along the minor and major axes. Based to our geometric and physical parameter settings, we find that the minimum thermal stability for the magnet sizes we consider is $29.5k_B T$, corresponding to a retention time of $6.7 \times 10^3 s$, which is adequate for the circuit switching frequencies considered in this work. The impact of \vec{H}_d is incorporated in factor f_{sw} in Equation (8).

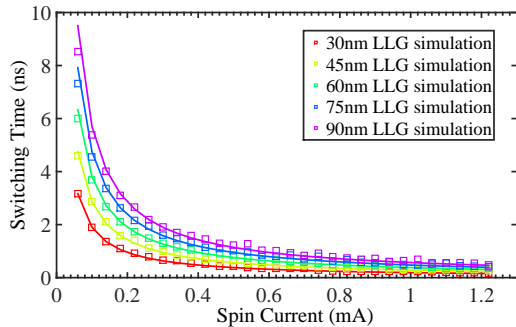


Fig. 4. LLG simulation results and corresponding curves from analytical equations with $f_{sw} = 4.7$ for relation between t_{sw} and I_s under various magnet lengths (15nm, 30nm, 45nm, 60m, and 75nm).

In order to precharacterize the factor f_{sw} and determine how it varies with ASL geometries, we design a series of simulations to examine the influence of magnet geometries to the relation between switching time t_{sw} and spin current I_s . We choose a discrete set of magnet lengths in the range from 30nm to 100nm. The parameters we used in the simulations are the same with those given later in Table I in Section V-A with the damping factor $\alpha = 0.007$ [2].

As shown in Figure 4, the switching time t_{sw} under a series spin currents I_s for various magnet lengths is obtained through

LLG simulations and denoted by square markers. A data fitting procedure was then performed based on Equation (8), and the best fit, shown by the continuous curves in the figure, is seen to match the data points well at each magnet size. For the specific parameters used in this experiment, we obtained $f_{sw} = 4.7$, and the figure demonstrates that f_{sw} does not change significantly with geometry, i.e., the geometric impact through \vec{H}_d is minimal.

Therefore, from Equations (8) and (11),

$$t_{sw} = \frac{l_{m,2} \left[\left(1 + \frac{k_2}{l_{m,1}}\right) \left(1 + \frac{k'_2}{l_{m,2}}\right) - e^{-\frac{2L}{\lambda N}} \right] (r_1 + r_2 l_{m,1})}{k'_1 V_{dd} e^{-\frac{L}{\lambda N}}} \quad (12)$$

where k'_1 modifies k_1 to capture the constants in $2f_{sw}qN_s$.

IV. OPTIMIZATION

The net conclusion of our analysis in Equation (12) is that the switching time t_{sw} of an ASL inverter stage

- reduces sublinearly with $l_{m,1}$,
- increases linearly with $l_{m,2}$, and
- reduces by an exponential dependence with L .

Therefore, the switching delay can be improved by adjusting the sizes of the magnets and reducing the length of the channel. For a global interconnect of fixed length, the insertion of buffers/inverters can reduce switching times by reducing channel lengths between buffers, with overheads due to the intrinsic delays of individual buffers. We now develop optimization formulations for an ASL buffer chain and a general circuit.

A. Optimization of an ASL buffer chain

1) *Problem formulation:* We now present an optimization formulation that optimizes the energy and delay of a long wire, driven by an ASL buffer and feeding an ASL load, through buffer insertion and sizing. We keep the width of each magnet constant, setting it to the width of the channel for better spin injection into the channel, and optimize the lengths of the magnets. The insertion of n buffers divides the wire of length L into $n + 1$ stages of length $L_i, 1 \leq i \leq n + 1$. In the i^{th} stage, we denote the input magnet length by $l_{m,i}$ and the output magnet length by $l_{m,i+1}$; note that the output magnet for the i^{th} channel also serves as the $(i + 1)^{\text{th}}$ input magnet.

Denoting the delay from the i^{th} to the $(i + 1)^{\text{th}}$ buffer in the buffer chain as $T_i(l_{m,i}, l_{m,i+1}, L_i)$, the total delay is:

$$T_{tot} = \sum_{i=1}^{n+1} T_i(l_{m,i}, l_{m,i+1}, L_i) \quad (13)$$

and the total energy over a clock period of P_{clc} is:

$$E_{tot} = \left(\sum_{i=1}^{n+1} V_{dd} I_{c,i} \right) P_{clc} \quad (14)$$

The optimization problem can be formulated as minimizing the energy over a delay constraint related to P_{clc} , as:

$$\begin{aligned} & \text{minimize}_{l_{m,i}, L_i} \quad \left(\sum_{j=1}^{n+1} V_{dd} I_{c,j} \right) \\ & \text{subject to} \quad \sum_{i=1}^{n+1} T_i(l_{m,i}, l_{m,i+1}, L_i) \leq P_{clc} \end{aligned} \quad (15)$$

2) *Buffer optimization as a posynomial programming problem*: In this section, we consider a simpler and more practical version of the optimization problem in (15), using equal channel lengths, and then optimizing the magnet lengths. We show that for the buffer chain, the total delay and the energy consumption of the ASL circuit are both posynomial functions, which implies that the optimization problem is a posynomial program [15] that can be solved to find the length of each magnet as well as the interconnect length in each stage. These problems can be efficiently solved with concrete guarantees of optimality since, unlike general nonlinear optimization problems, posynomial programs possess the property that any local minimum is a global minimum. In Section V, we will use a posynomial program solver, `gpposy` from the geometrical programming optimizer `GGPLAB` [16] to optimize these ASL circuits. To the best of our knowledge, this is the first time this problem has been formulated as a posynomial program.

For a buffer chain with n magnets inserted between input and output magnets, we denote the length of the i^{th} magnet by $l_{m,i}$ and assume that the channel length between two magnets is equal, i.e., $L_i = L/(n+1)$, and the magnet width is constant and set to the minimum value. The total delay for the buffer chain can be obtained from Equation (12) and (13) as:

$$T_{tot} = \frac{1}{k'_1 V_{dd} e^{-L_i/\lambda_N}} \left(\sum_{i=1}^{n+1} l_{m,i+1} (r_1 + r_2 l_{m,i}) \cdot \left[\left(1 + \frac{k_2}{l_{m,i}} \right) \left(1 + \frac{k'_2}{l_{m,i+1}} \right) - e^{-2L_i/\lambda_N} \right] \right) \quad (16)$$

Assuming the buffer chain is run at its fastest speed, with $P_{clc} = T_{tot}$, then the total energy E_{tot} for the buffer chain is derived from Equations (10), (12), and (14) as:

$$E_{tot} = \frac{V_{dd}}{k'_1 e^{-L_i/\lambda_N}} \left(\sum_{i=1}^{n+1} \frac{l_{m,i}}{r_1 + r_2 l_{m,i}} \right) \left(\sum_{i=1}^{n+1} l_{m,i+1} \cdot (r_1 + r_2 l_{m,i}) \left[\left(1 + \frac{k_2}{l_{m,i}} \right) \left(1 + \frac{k'_2}{l_{m,i+1}} \right) - e^{-2L_i/\lambda_N} \right] \right) \quad (17)$$

In Equation (16) and (17), if we take T_{tot} and E_{tot} as functions of $l_{m,i}$, the coefficients for all terms that include $l_{m,i}$ are always positive. Therefore, both functions are posynomial. It can be shown that even when the L_i values are not uniform, these are posynomial functions in $l_{m,i}$ and L_i .

For a more specific case where all magnets are assumed to have the same length, i.e., $l_{m,i}$ is the same for all i , it is possible to find a closed form minimum for the delay of the buffer chain. Using Equation (16), the delay for the optimal l_m can be shown as:

$$T_{tot} = \frac{n+1}{k'_1 V_{dd} e^{-\frac{L_i}{\lambda_N}}} \left(\frac{r_2 k_2 k'_2}{l_m} + \left[r_1 (1 - e^{-\frac{2L_i}{\lambda_N}}) + r_2 k_2 + r_2 k'_2 \right] l_m + r_2 (1 - e^{-\frac{2L_i}{\lambda_N}}) l_m^2 + r_1 k_2 + r_1 k'_2 + r_2 k_2 k'_2 \right) \quad (18)$$

Note that in the above formulation all the coefficients of l_m are positive and therefore it is a polynomial of l_m , leading to a closed form solution of l_m for minimum delay.

B. Formulation for a general circuit

We now consider the sizing problem without buffer insertion for a user-specified clock period, P_{clc} . The energy consumed by an ASL circuit over the clock period is the summation of contributions over all gates in the circuit:

$$E_{tot} = \left(\sum_j V_j I_{c,j} \right) P_{clc} \quad (19)$$

The optimization problem of geometries for an ASL circuit to give minimum delay under certain delay requirement is:

$$\begin{aligned} & \text{minimize}_{l_{m,i}, L_i} \quad \sum_j V_j I_{c,j} \\ & \text{subject to} \quad T_{tot} \leq P_{clc} \end{aligned} \quad (20)$$

where T_{tot} is the delay of the critical path.

In order to explore the maximum amount of delay reduction that can be achieved through the optimization, we propose an optimization algorithm for general circuits and its pseudocode is shown in Algorithm 1. It solves the above formulation using a variant of the TILOS algorithm [17].

Algorithm 1 Geometric optimization for ASL circuit

Input: Circuit netlist and placement result;
Incremental length multiplier α .
Output: Delay, energy consumption and sizes of magnets.
1: Compute initial circuit delay T_0 and critical path.
2: $T_{min} \leftarrow T_0$.
3: $i \leftarrow 1$.
4: **repeat**
5: **for** each magnet j on critical path **do**
6: **if** $l_j \times \alpha < l_{upper-bound}$ **then**
7: Calculate the sensitivity $\partial Delay_j / \partial Power_j$ from sizing magnet j .
8: **end if**
9: **end for**
10: Identify the magnet k with the most negative sensitivity.
11: $l_k \leftarrow l_k \times \alpha$.
12: Compute corresponding circuit delay T_i and new critical path.
13: $T_{min} \leftarrow T_i$.
14: $i \leftarrow i + 1$.
15: **until** $T_i \geq T_{min}$.

Line 1 calculates the initial delay of the circuit based on the netlist and ASL gate and interconnect delays (Section II-B) and finds out the critical path. Initial assignment for the minimum circuit delay is performed in lines 2–3. Next, lines 5–9 compute the sensitivity, $\partial Delay_j / \partial Power_j$, for each magnet in the gates on the critical path if its size will not exceed the upper-bound of magnet size $l_{upper-bound}$ after being sized up. This sensitivity is numerically achieved by upsizing one magnet by a geometric factor α at a time and calculating the delay reduction and power increase caused by changing this single magnet. By our algorithm, delay of the circuit is reduced with the minimal amount of power penalty. Line 10 then finds out the magnet with largest impact on circuit delay and sizes it up by a factor α to get the largest delay improvement for the smallest overhead (line 11). The circuit delay in iteration i is updated as T_i (lines 12–13), and the process continues until the stopping criterion is met when no more delay improvement can be made (lines 4, 14–15). This provides the tradeoff curve of interest.

V. RESULTS

A. Simulation parameters

We present some material and geometric parameters used in our simulations in Table I. These parameters, chosen in con-

sultation with technologists, are intended to be representative and indicative of current and future technologies.

To realistically estimate the ohmic loss of the power delivery network in Equation (1), we evaluated a standard set of power grid benchmarks [18], and determined that the effective resistance from each pin to the supply node is on the order of 0.25Ω . Since these benchmarks evaluate the top few layers of a power grid (a typical number is five layers), we multiply this number by $2\times$ to model the impact of lower metal layers. Therefore, we use an effective resistance of 0.5Ω each for the supply and the ground line. This effective resistance is effectively translated into a dimension of $140\text{nm}\times 140\text{nm}\times 1400\text{nm}$ in width, thickness, and length, respectively, where the cross-sectional dimensions are based on [19]. We note that for an efficient ASL implementation, it is essential for the power grid resistance to be around this value, which is lower than the corresponding value for CMOS technologies. This is because $R_m + R_n \approx 7\Omega$, and if $R_s + R_g$ is much larger, then a large fraction of power will be wastefully dissipated in the power grid resistors.

TABLE I
MATERIAL AND GEOMETRIC PARAMETERS.

Parameter	Value
M_s (saturation magnetization)	$780 \times 10^3 \text{A/m}$ [2]
ρ_F (resistivity of magnet)	$170\Omega\cdot\text{nm}$ [2] [20]
ρ_N (resistivity of channel)	$7\Omega\cdot\text{nm}$ [2] [20]
w_m (width of magnet)	10nm
t_m (thickness of magnet)	5nm
w_n (width of channel)	20nm
t_n (thickness of channel)	30nm

For parameters that most closely affect performance metrics, recognizing that the technology is rapidly evolving today, we explore a range of values in our experiments that reflect various technology scenarios to reflect current-day and project future technologies. In our experiments, the value of λ_F is chosen in the range of 5nm to 50nm [4] [20], and the polarization factor P from 0.5 to 0.7 [11]. The channel spin diffusion length, λ_N , can take values in a large range since various materials could be considered [21]. Given this background and the strong materials research in this area, we choose two possible values of λ_N of 450nm and 1000nm, which could represent the spin diffusion lengths of bulk copper under room temperature and low temperature from various experimental measurements [21], [22]. However, as pointed out by [22] and [23], the spin diffusion length will degrade significantly due to size effects. Therefore, two more sets of simulations with λ_N of 180nm and 400nm are added, corresponding to a degradation to 40% of the bulk values, estimated under the channel dimensions in our work through the results shown in [22]. The supply voltage is chosen in 10mV–30mV range [2]. It is unrealistic to show results for all cross-products of these choices, and we focus on two parameter sets with bulk and degraded spin diffusion lengths in Table II: from parameter set 1, a nearer-term technology, to set 2 for projected technologies and with higher V_{dd} .

We calculate switching time and energy, static timing analysis, and optimizations using MATLAB and C++ on a 2.53

GHz Intel Core i3 with 4GB RAM.

TABLE II
THREE PARAMETER CHOICES FOR P , λ_N , AND V_{dd} .

Values of technology nodes		
Parameter set	1	2
P (magnet polarization factor)	0.5	0.6
λ_N (spin diffusion length, bulk / degraded, nm)	450 / 180	1000 / 400
V_{dd} (supply voltage, mV)	10	30
w_c (channel width, nm)	10	20
t_c (channel thickness, nm)	20	30

B. Optimizing a buffered wire

We provide a simple example of a ASL buffer chain to illustrate the use of the posynomial formulation to individually optimize the size of each magnet. A total interconnect length of 1800nm is considered with nine equally-spaced buffers inserted between the input and output magnets. We consider the spin diffusion length of magnet $\lambda_F = 14.5\text{nm}$ [21], channel width $w_n = 20\text{nm}$, and thickness $t_n = 30\text{nm}$. The length of the input magnet and output magnet are both set to 30nm. The posynomial formulation is fed to the GGPLAB solver [16], which optimizes the length of each magnets to minimize the delay of the entire buffer chain. These optimized lengths (chosen to be multiples of the feature size, 10nm) are shown in Table IV for the case when 9 buffers are inserted.

TABLE IV
OPTIMIZED MAGNET LENGTHS (NM) FOR MINIMAL DELAY ON A LINE WITH 9 BUFFERS BETWEEN FIXED-SIZE INPUT AND OUTPUT MAGNETS.

In	1	2	3	4	5	6	7	8	9	Out
30	80	90	90	100	100	100	100	100	90	30

Next, we repeat these posynomial programming optimizations for a set of buffer chains with a varying number of buffers under the above technology parameters based on optimization (15). For a specified number of equally-spaced buffers (n), we provide the delay and corresponding energy under three cases in Fig. 5: (i) *Optimized delay*: the length of each magnet is sized individually for optimal delay; (ii) *Closed-form delay*: All the inserted magnets are assumed to have the same length, i.e., $l_{m,i} = l_{m,i+1} = l_m$, except for the first and last magnet in the buffer chain, whose lengths are fixed. In this case the delay is very similar to the situation described in Equation (18) and a closed form solution of l_m can still be found for the minimum delay; (iii) *Unoptimized delay*: The lengths of all inserted magnets are of minimum length 30nm, i.e., no optimization is performed. The nature of these curves is similar for each value of the spin diffusion length in Table II, and we choose a representative value of 400nm to illustrate the results. The zero buffer case is not considered as it cannot supply the critical spin current, I_s^{cr} , required for switching the output [2].

As shown in Figure 5(a), the minimum delay occurs when four magnets are inserted, corresponding to a delay of 37.6ns for the case where each inserted magnet is sized individually.

TABLE III
 DELAY BEFORE OPTIMIZATION (UNSIZED), DELAY AFTER OPTIMIZATION (SIZED), IMPROVEMENT IN PERCENTAGE, AND RUNTIME OF OPTIMIZATION PROGRAM UNDER TWO PARAMETER SETS WITH BULK / DEGRADED λ_N OF CHANNEL MATERIAL FOR THE ISCAS-85 BENCHMARKS.

Ckt.	Parameter Set 1				Parameter Set 2			
	Unsize Delay (ns)	Sized Delay (ns)	Improvement (%)	Runtime (s)	Unsize Delay (ns)	Sized Delay (ns)	Improvement (%)	Runtime (s)
C17	39.2 / 45.1	30.0 / 33.5	23.5 / 25.7	0.10 / 0.16	5.75 / 7.19	3.77 / 4.61	34.4 / 35.9	0.10 / 0.14
C432	422.0 / 495.1	352.8 / 402.8	16.4 / 18.6	5.03 / 14.7	58.0 / 72.9	41.0 / 50.8	29.3 / 30.3	8.1 / 11.1
C499	418.5 / 498.9	360.4 / 415.1	13.9 / 16.8	5.74 / 42.4	50.8 / 66.1	37.9 / 48.4	25.4 / 26.8	19.2 / 39.6
C880	374.6 / 441.0	316.5 / 363.9	15.5 / 17.5	3.20 / 11.1	49.8 / 63.2	35.7 / 44.6	28.3 / 29.4	4.1 / 7.8
C1355	352.8 / 418.9	297.9 / 345.0	15.6 / 17.6	20.7 / 68.6	45.2 / 57.7	32.8 / 41.4	27.4 / 28.2	31.3 / 57.2
C1908	481.2 / 567.2	407.6 / 465.1	15.3 / 18.0	14.8 / 54.8	63.7 / 79.2	46.0 / 56.7	27.8 / 28.4	25.4 / 44.1
C2670	427.7 / 509.0	367.3 / 427.5	14.1 / 16.0	4.07 / 18.8	49.5 / 64.9	37.1 / 48.0	25.1 / 26.0	7.3 / 15.6
C3540	647.1 / 763.8	549.7 / 630.1	15.1 / 17.5	17.2 / 53.5	83.3 / 106.2	60.7 / 75.9	27.1 / 28.5	32.9 / 52.1
C5315	551.7 / 646.9	468.0 / 536.0	15.2 / 17.1	11.5 / 45.1	70.9 / 89.6	51.1 / 64.2	28.9 / 28.3	21.4 / 38.3
C6288	1384.7 / 1610.3	1161.9 / 1305.2	16.1 / 18.9	158.8 / 412.3	198.4 / 242.0	141.8 / 169.5	28.5 / 30.0	369.6 / 499.4
C7552	662.7 / 793.3	573.6 / 668.5	13.4 / 15.7	20.0 / 82.1	77.6 / 101.0	58.0 / 74.8	25.3 / 25.9	25.6 / 64.6

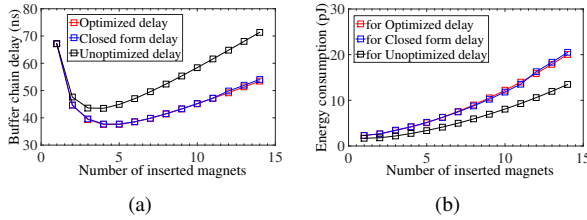


Fig. 5. The (a) delay and (b) energy of the buffer chain under three different cases vs. number of inserted buffers.

As a comparison, the delay with the same number of unsized magnet insertion is 44.9ns, implying that the optimization provides a 16.3% improvement with only a small energy overhead, as shown in Fig. 5(b). It is also observed that when all magnets are identically sized, the delay curve virtually coincides with that for the individually-sized case. Therefore, the closed form is a fast predictor for the optimal delay.

It is noteworthy that these optimizations employ the analytical method described in Section II-B. An alternative to analytical modeling is the MNA-based modeling method described in Section II-C1. Although the results obtained by these two modeling methods are close to each other only under certain specific conditions, the analytical modeling method shows a good fidelity in finding minimum delay and is therefore very useful for delay optimization. Further details about the comparison of the two modeling methods and the notion of fidelity are provided in the Supplementary Material.

C. Optimization of benchmark circuits

In order to demonstrate the feasibility and the benefits of our optimization methods on general ASL circuits, we tested Algorithm 1 on ISCAS85 benchmark circuits. The benchmarks are placed using CAPO placement tool [24], using an estimation of the ASL cell area, with magnet lengths changed at a granularity of 10nm steps.

A buffer insertion step is performed for any interconnect longer than L_0 to strengthen the signal before the circuit is optimized through Algorithm 1. In the optimization for ISCAS benchmarks, we choose L_0 to be equal to λ_N , because in the π model for the channel mentioned in Section II-C1, the spin signal loss will be close to saturation when the ratio

L/λ_N exceeds 1. The row utilization leaves sufficient space for inserting buffers and sizing these cells.

Two sets of parameters, representing two technologies as shown in Table II are used. The delay before optimization, after optimization, improvement in percentage, and the runtime for each benchmark under the two technology parameter sets with bulk and degraded spin diffusion lengths are shown in Table III. Although the degradation of spin diffusion length will inevitably induce higher delay, optimization through sizing could still bring a good amount of improvements for all circuit benchmarks, indicating the effectiveness and robustness of our algorithm across various technologies. Various techniques have been applied to enhance the efficiency of Algorithm 1, including the use of a precharacterized look-up table for intrinsic delay of ASL gates and incremental timing analysis after a change in the TILOS-like optimization algorithm. It can be seen from Table III that the more advanced technologies have shorter delays and larger delay improvements with reasonable runtime on the ISCAS85 benchmark circuits.

Detailed results are presented for the C6288 benchmark under the two technology parameters with bulk and degraded spin diffusion lengths of Table II to demonstrate the effectiveness of our optimization algorithm. The delay-power trade-off curve under parameter set 1 is shown in Fig. 6(a). The optimization begins at the highest delay, at the right of the curve. As the delay reduces through the optimization, the power increases as a penalty. The delay reduction and energy for C6288 benchmark is shown in Fig. 6(b) and clearly through each iteration, the delay of the circuit keeps decreasing. The energy, however, behaves differently. At the beginning of the optimization, it decreases together with delay since sizing the gates helps overcome gross inefficiencies in the interconnect bottleneck. The reduction of delay dominates the power increase in the power-delay product at this moment. As the benefit of delay reduction becomes smaller as the optimization proceeds, the increase in power finally dominates and the energy starts to increase. Similar trends are seen under three other sets of results. The trend of power-delay curves indicates that at the beginning of the optimization, power is relatively insensitive to upsizing of the magnets, yet as the magnets on the critical path become larger and are still sized up for smaller delay, power becomes more sensitive to sizing.

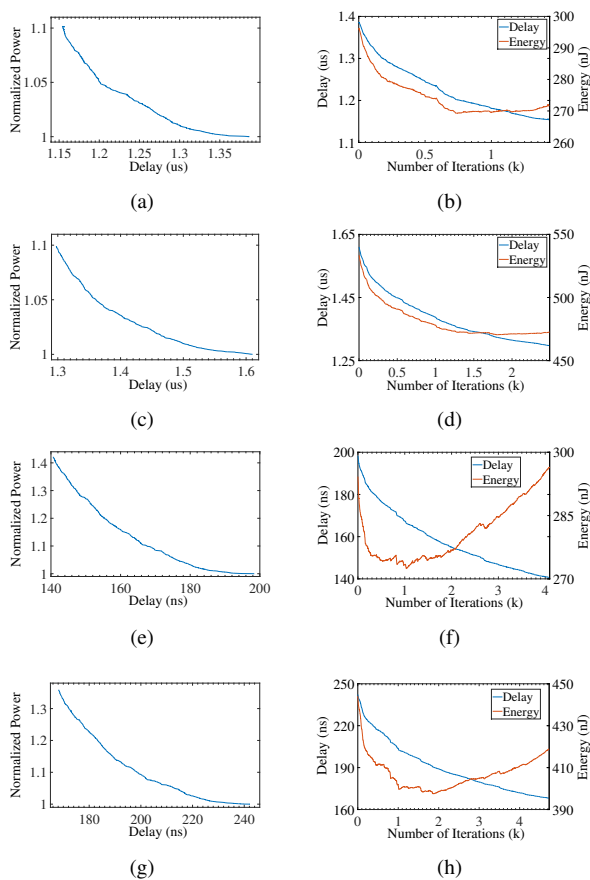


Fig. 6. Relation between delay and power C6288 through optimization (left) and change in delay and energy through optimization iterations (right). (a), (b): parameter set 1 with bulk spin diffusion length of 450nm; (c), (d): parameter set 1 with degraded spin diffusion length of 180nm; (e), (f): parameter set 2 with bulk spin diffusion length of 1000nm; (g), (h): parameter set 2 with degraded spin diffusion length of 400nm.

VI. CONCLUSION

This paper has explored the energy/delay trade-off relation and presented a systematic approach to optimizing ASL circuits. We have presented a posynomial programming approach for buffered lines and a numerical optimization scheme for general circuits. Under realistic parameters that include factors such as degradation in the spin diffusion length due to scaling, our results demonstrate the utility of sizing ASL circuits to reduce delay by about 30%. This framework can enable technology-circuit codesign by allowing the evaluation of technology parameters on circuit performance.

ACKNOWLEDGMENT

The authors are grateful to M. Mankalale, V. Mishra, J. Hu, A. Smith, and J. Wang for helpful discussions and input into this work. This work was supported in part by C-SPIN, one of six centers of STARnet, a Semiconductor Research Corporation program, sponsored by MARCO and DARPA.

REFERENCES

[1] B. Behin-Aein, D. Datta, S. Salahuddin, and S. Datta, "Proposal for an all-spin logic device with built-in memory," *Nature Nanotechnology*, vol. 5, no. 4, pp. 266–270, 2010.

[2] B. Behin-Aein, A. Sarkar, S. Srinivasan, and S. Datta, "Switching energy-delay of all spin logic devices," *Applied Physics Letters*, vol. 98, no. 12, pp. 123 510–1–123 510–3, 2011.

[3] B. Behin-Aein, A. Sarkar, and S. Datta, "Modeling circuits with spins and magnets for all-spin logic," in *Proceedings of the European Solid-State Device Research Conference (ESSDERC)*, 2012, pp. 36–40.

[4] S. Manipatruni, D. E. Nikonov, and I. A. Young, "Circuit theory for spice of spintronic integrated circuits," *arXiv preprint arXiv:1112.2746*, 2011.

[5] S. Manipatruni, D. E. Nikonov, I. Young *et al.*, "Modeling and design of spintronic integrated circuits," *IEEE Transactions on Circuits and Systems I: Regular Papers*, vol. 59, no. 12, pp. 2801–2814, 2012.

[6] S. Srinivasan, V. Diep, B. Behin-Aein, A. Sarkar, and S. Datta, "Modeling multi-magnet networks interacting via spin currents," *arXiv preprint arXiv:1304.0742*, 2013.

[7] S.-C. Chang, S. Dutta, S. Manipatruni, D. Nikonov, I. Young, and A. Naeemi, "Interconnects for all-spin logic using automation of domain walls," *Exploratory Solid-State Computational Devices and Circuits, IEEE Journal on*, vol. 1, pp. 49–57, 2015.

[8] S. Rakheja and A. Naeemi, "Interconnection aspects of spin torque devices: Delay, energy-per-bit, and circuit size modeling," in *Proceedings of the IEEE International Symposium on Quality Electronic Design*, 2011, pp. 1–9.

[9] C. Augustine, G. Panagopoulos, B. Behin-Aein, S. Srinivasan, A. Sarkar, and K. Roy, "Low-power functionality enhanced computation architecture using spin-based devices," in *Proceedings of the IEEE/ACM International Symposium on Nanoscale Architectures (NANOARCH)*, 2011, pp. 129–136.

[10] S. Rakheja and A. Naeemi, "Interconnect analysis in spin-torque devices: Performance modeling, optimal repeater insertion, and circuit-size limits," in *Proceedings of the IEEE International Symposium on Quality Electronic Design*, 2012, pp. 283–290.

[11] S. Takahashi and S. Maekawa, "Spin current in metals and superconductors," *Journal of the Physical Society of Japan*, vol. 77, no. 3, pp. 031 009–1–013 009–14, 2008.

[12] J. C. Slonczewski, "Current-driven excitation of magnetic multilayers," *Journal of Magnetism and Magnetic Materials*, vol. 159, no. 1, pp. L1–L7, 1996.

[13] D. E. Nikonov, G. I. Bourianoff, G. Rowlands, and I. N. Krivorotov, "Strategies and tolerances of spin transfer torque switching," *Journal of Applied Physics*, vol. 107, no. 11, p. 113910, 2010.

[14] A. Aharoni, "Demagnetizing factors for rectangular ferromagnetic prisms," *Journal of Applied Physics*, vol. 83, no. 6, pp. 3432–3434, 1998.

[15] J. G. Ecker, "Geometric programming: methods, computations and applications," *SIAM Review*, vol. 22, no. 3, pp. 338–362, 1980.

[16] A. Mutapcic, K. Koh, S. Kim, L. Vanden-Berghe, and S. Boyd, "GGPLAB: A simple matlab toolbox for geometric programming," <http://stanford.edu/~boyd/ggplab/>, 2006.

[17] J. Fishburn and A. Dunlop, "TILOS: A polynomial programming approach to transistor sizing," in *Proceedings of the IEEE International Conference on Computer-Aided Design*, 1985, pp. 326–328.

[18] Z. Li, P. Li, and S. R. Nassif, "Ibm power grid benchmarks," accessed December 18, 2015.

[19] "FreePDK 45nm open-access based PDK for the 45nm technology node," <http://www.eda.ncsu.edu/wiki/FreePDK>.

[20] T. Kimura, T. Sato, and Y. Otani, "Temperature evolution of spin relaxation in a nife/cu lateral spin valve," *Physical review letters*, vol. 100, no. 6, p. 066602, 2008.

[21] J. Bass and W. P. Pratt Jr, "Spin-diffusion lengths in metals and alloys, and spin-flipping at metal/metal interfaces: an experimentalist's critical review," *Journal of Physics: Condensed Matter*, vol. 19, no. 18, p. 183201, 2007.

[22] S. Rakheja, S.-C. Chang, and A. Naeemi, "Impact of dimensional scaling and size effects on spin transport in copper and aluminum interconnects," *IEEE Transactions on Electron Devices*, vol. 60, no. 11, pp. 3913–3919, 2013.

[23] M. Erekhinsky, A. Sharoni, F. Casanova, and I. K. Schuller, "Surface enhanced spin-flip scattering in lateral spin valves," *Applied Physics Letters*, vol. 96, no. 2, p. 022513, 2010.

[24] J. A. Roy, D. A. Papa, S. N. Adya, H. H. Chan, A. N. Ng, J. F. Lu, and I. L. Markov, "Capo: robust and scalable open-source min-cut floorplacer," in *Proceedings of the International Symposium on Physical Design*, 2005, pp. 224–226.

[25] L. O. Chua and P.-M. Lin, *Computer-aided analysis of electronic circuits: Algorithms and computational techniques*. Englewood Cliffs, NJ: Prentice-Hall, 1975.

SUPPLEMENTARY MATERIAL

S.1 SPIN TRANSFER THROUGH THE CHANNEL USING
MODIFIED NODAL ANALYSIS

S.1.1 A numerical model for modeling ASL circuit performance

An alternative to the analytical model mentioned in Section II-B is a numerical method, based on Modified Nodal Analysis (MNA), which enables fast simulations for spintronic circuits and can handle more complicated structures in the spintronic circuits [2], [4]–[6]. In this section we will briefly review this modeling method and show how to use it to calculate the spin injection efficiency in the non-local spin valve structure. The spin injection efficiency in the ASL inverter can be calculated in a similar way.

For each component in the non-local spin valve structure, a π -network of conductance matrices can be constructed. Every π -network is composed of two kinds of matrices: (a) a series conductance matrix that captures the relation between charge/spin voltage drop and charge/spin current and (b) a shunt conductance matrix that captures the dissipation of spin current. We focus on two types of components for (I) the ferromagnet and (II) the non-magnetic channel and only present the 2x2 matrix formulation mentioned in [6].

S.1.1.1 π -network of conductance matrices for ferromagnet: For the ferromagnet, its series and shunt matrices are of the following form:

$$G_F^{se} = \frac{1}{\rho L} \begin{pmatrix} 1 & p \\ p & p^2 + \alpha \operatorname{csch}\left(\frac{L}{\lambda_F}\right) \end{pmatrix}, \quad (21)$$

$$G_F^{sh} = \frac{1}{\rho L} \begin{pmatrix} 0 & 0 \\ 0 & \alpha \tanh\left(\frac{L}{2\lambda_F}\right) \end{pmatrix} \quad (22)$$

where $\alpha = (1 - p^2) \left(\frac{L}{\lambda_F}\right)$ with p being the polarization factor of the magnet, L being the length along the current propagation direction of the magnet, and λ_F being the spin diffusion length of the magnet. Note that the off-diagonal components in the G_F^{se} indicate a coupling relation between charge and spin voltages/currents.

S.1.1.2 π -network of conductance matrices for non-magnetic channel: For the non-magnetic channel, its series and shunt matrices are of the following form:

$$G_N^{se} = \frac{1}{\rho L} \begin{pmatrix} 1 & 0 \\ 0 & \left(\frac{L}{\lambda_N}\right) \operatorname{csch}\left(\frac{L}{\lambda_N}\right) \end{pmatrix}, \quad (23)$$

$$G_N^{sh} = \frac{1}{\rho L} \begin{pmatrix} 0 & 0 \\ 0 & \left(\frac{L}{\lambda_N}\right) \tanh\left(\frac{L}{2\lambda_N}\right) \end{pmatrix} \quad (24)$$

where L being the length of the non-magnetic channel along the direction that current propagates, and λ_N is the spin diffusion length of the non-magnetic channel. The zeros in the off-diagonal positions of matrix G_N^{se} imply that there is no coupling between charge and spin quantities in the non-magnetic channel.

S.1.1.3 Non-local spin valve structure represented by π -network conductance matrices: With the above formulation for each component in the non-local spin valve structure, a representation for this structure can be constructed. The

corresponding structure for the basic ASL gate from Fig. 2 is shown in Fig. 7. The element stamps for all components in the structure, described in the two sections above, can be combined using a routine approach that creates the MNA equations [25] to solve for the unknowns, i.e., the charge/spin current and voltage in the structure.

Our analysis uses this method to calculate the spin injection efficiency, which is the ratio of the output spin current through magnet F2 versus the input charge current through magnet F1 as in Fig. 7. This modeling method is also convenient for calculations of quantities in complicated ASL structures as we show in Section II-C1. This is used to determine the spin torque current that switches the output magnet, and is further used to determine the gate delay.

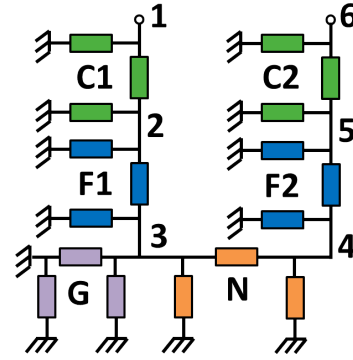


Fig. 7. Inverter structure represented by π -network conductance matrices.

S.1.2 Differences between analytical method and MNA method

In the paper, we have used two methods for modeling ASL circuits, one based on an analytical model, and another based on a numerical method derived from MNA. Due to its algebraic form, the analytical method is helpful in analyzing the trends and impacts of the material or geometrical parameters to the performance of ASL circuits. However, it is limited to single fanout circuits, and the MNA modeling method is more convenient and flexible in performing numerical analysis of complicated ASL structures with multiple fanouts.

These two methods are fundamentally the same, and both originate from the description of the diffusion behaviors for the two types of spins [2], [11]. However, as pointed out in [11], the analytical derivation makes the assumption that the thickness of the input and output magnets is much larger than the spin diffusion length of the magnet material. This assumption was valid in the experimental case considered in their paper and may not apply here since we are trying to explore a larger design space for the dimensions of the ASL structures where the magnets have very small geometries. Due to the influence of this assumption, a performance metric of interest under these two models may evaluate to inconsistent values under certain cases. In this section, we provide a numerical analysis of some discrepancies between these two methods for key performance metrics in an ASL structure.

Fig. 8 shows the difference between the spin injection efficiency by these two modeling methods under various ratio of magnet thickness versus its spin diffusion length λ_F . It

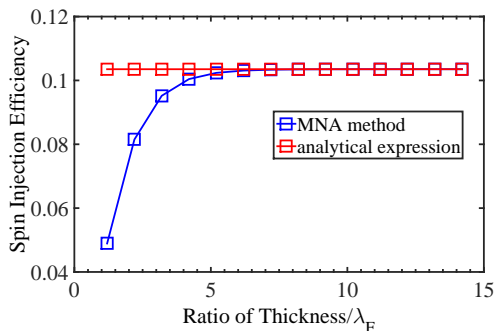


Fig. 8. Spin injection efficiency by two modeling methods under various ratio of magnet thickness versus spin diffusion length of magnet λ_F .

is seen that if the magnet thickness is greater than $4\lambda_F$, the discrepancies from two models start to become negligible.

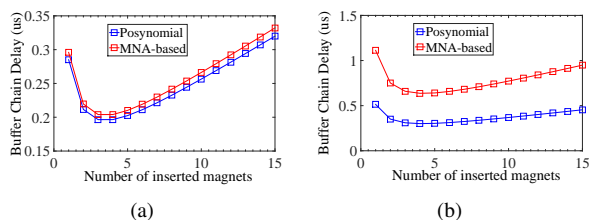


Fig. 9. The buffer chain delay optimization results generated by the analytical and MNA-based modeling methods under a magnet thickness of 20nm with a spin diffusion length of (a) $\lambda_F = 5\text{nm}$ and (b) $\lambda_F = 15\text{nm}$.

Going beyond the spin injection efficiency to system-level performance, we examine the impact of using the analytical or MNA models for optimizing buffered wires under our approach. Given a total interconnect of fixed length (L_{tot}) between the input and output magnets, we vary the number of buffers in the line, keeping the buffers equally spaced on the line. Under the simulation parameters in Table I and the same experimental setting as in Section V-B, we optimize the lengths of inserted magnets individually to achieve the optimal delay for the entire buffered wire under two separate delay models: the analytical modeling method and the MNA-based modeling method.

Fig. 9 shows the optimal delays of a buffered wire, as the number of buffers is increased, under these two delay models. The magnet thickness is fixed at 20nm, but we perform the analyses under two different values for the spin diffusion length, λ_F . In Fig. 9(a), $\lambda_F = 5\text{nm}$, i.e., the thickness of magnet is $4\lambda_F$, while in Fig. 9(b), $\lambda_F = 15\text{nm}$, i.e., the magnet thickness is $4/3\lambda_F$. In Fig. 9(a), the percentage improvements of optimal delay by MNA method and posynomial formulation are 63.1% and 64.4% respectively, while in Fig. 9(b), the percentage improvements are 51.1% and 76.9% respectively. The differences between two methods are 1.3% and 25.8%, which indicates that the MNA method and posynomial formulation are more close to each other when the thickness of magnet is much larger than spin diffusion length of ferromagnet λ_F .

As predicted by Fig. 8, the curves in Fig. 9(a) closely track each other and the optimum point is roughly equal, both in terms of the number of magnets and the delay at each point.

As expected, the analytical method has an advantage in terms of speed of evaluation. Similarly, as expected, in Figure 9(b), where the λ_F is larger, the results from two modeling methods are quite different from each other. However, interestingly, their trends for this case remain roughly the same under both models: the minimum delay corresponds to the case where three buffers are chosen. In other words, although the analytical method does not provide the same prediction on the optimal result as the more accurate MNA method, it has good *fidelity* with the final result. Therefore, it can still be used to analyze the minimal value. Due to its closed form, the analytical form is of great utility in assisting designers to explore the optimal performance of this circuit, and it can enable fast optimization (e.g., using geometric programming).

S.2 AN EXPRESSION FOR t_{sw} FROM THE SOLUTION OF THE LLG EQUATION

In this section, we discuss the approach in [2], with some minor modifications, for evaluating t_{sw} based on solving the LLG equation. We are particularly interested this evaluation since it provides a convenient way to evaluate the switching time inexpensively without a full LLG solution. Taking the time-integral of the LLG equation over the switching time,

$$\int_0^{t_{sw}} \frac{d\vec{m}}{dt} dt = - \int_0^{t_{sw}} |\gamma| \vec{m} \times \vec{H}_{eff} dt + \int_0^{t_{sw}} \alpha \vec{m} \times \frac{d\vec{m}}{dt} dt - \int_0^{t_{sw}} \frac{1}{qN_s} \vec{m} \times (\vec{m} \times \vec{I}_s) dt \quad (25)$$

During switching, we focus on the change along the z axis: in its stable states, corresponding to two logic states, the magnetization aligns along this positive or negative direction. This axis is also called the easy axis since the magnetization is in its lowest energy state along it. For the z component, \vec{m}_z , of the normalized magnetization vector,

$$\int_0^{t_{sw}} \frac{d\vec{m}_z}{dt} dt = \int_{\mp 1}^{\pm 1} d\vec{m}_z = \pm 2, \quad \int_0^{t_{sw}} \alpha \left[\vec{m} \times \frac{d\vec{m}}{dt} \right]_z dt = 0 \quad (26)$$

If \vec{H}_{eff} only consists of the uniaxial anisotropy field \vec{H}_k , then the first term on the RHS of Equation (25) goes to zero. However, this is not the case when \vec{H}_{eff} also contains the demagnetizing field \vec{H}_d . This perturbation is captured by using a multiplier f_1 on the LHS of Equation (25) to obtain:

$$2f_1 q N_s = \int_0^{t_{sw}} [\vec{m} \times (\vec{m} \times \vec{I}_s)]_z dt \quad (27)$$

Assuming a constant spin current I_s during switching, and approximating $\vec{m} \times (\vec{m} \times \vec{I}_s) = I_s/f_2$, where f_2 is a constant factor the right hand side evaluates to $I_s t_{sw}/f_2$. Therefore, Equation (27) becomes $2f_1 q N_s = I_s t_{sw}$, where $f_{sw} = f_1/f_2$ is precharacterized by LLG simulations.

From Equation (3), writing the spin current at the end of the channel as $I_s = \eta I_c$, the switching time of the gate is:

$$t_{sw} = 2f_{sw} q N_s / (\eta I_c) \quad (28)$$

where I_c is given by Equation (1).

Based on this expression, we have evaluated f_{sw} in the paper and shown it to be independent of the magnet size over the optimization region.